AGU PUBLICATIONS

JGR

Journal of Geophysical Research: Planets

RESEARCH ARTICLE
10.1002/2016JE005093

Key Points:
- There is quantitative agreement in polar vortex structure in two Mars reanalyses
- There is near-zero PV equatorward of jet core, steepest meridional gradients poleward of jet, and maximum PV is offset from the pole
- On monthly timescale there is an elliptical annulus of potential vorticity but shape and orientation is much more variable at shorter times

Correspondence to:
D. W. Waugh,
Waugh@jhu.edu

Citation:
Waugh, D. W., A. D. Toigo, S. D. Guzewich, S. J. Greybush, R. J. Wilson, and L. Montabone (2016), Martian polar vortices: Comparison of reanalyses, *J. Geophys. Res. Planets*, *121*, 1770–1785, doi:10.1002/2016JE005093.

Received 27 MAY 2016
Accepted 30 AUG 2016
Accepted article online 5 SEP 2016
Published online 21 SEP 2016

Martian polar vortices: Comparison of reanalyses

D. W. Waugh[1], A. D. Toigo[2], S. D. Guzewich[3], S. J. Greybush[4], R. J. Wilson[5], and L. Montabone[6]

[1]Department of Earth and Planetary Sciences, Johns Hopkins University, Baltimore, Maryland, USA, [2]Department of Meteorology and Atmospheric Science, Johns Hopkins University Applied Physics Laboratory, Laurel, Maryland, USA, [3]CREST/USRA/NASA GSFC, Greenbelt, Maryland, USA, [4]Pennsylvania State University, University Park, Pennsylvania, USA, [5]NOAA GFDL, Princeton, New Jersey, USA, [6]Space Science Institute, Boulder, Colorado, USA

Abstract The structure and evolution of the Martian polar vortices is examined using two recently available reanalysis systems: version 1.0 of the Mars Analysis Correction Data Assimilation (MACDA) and a preliminary version of the Ensemble Mars Atmosphere Reanalysis System (EMARS). There is quantitative agreement between the reanalyses in the lower atmosphere, where Mars Global Surveyor (MGS) Thermal Emission Spectrometer (TES) data are assimilated, but there are differences at higher altitudes reflecting differences in the free-running general circulation model simulations used in the two reanalyses. The reanalyses show similar potential vorticity (PV) structure of the vortices: There is near-uniform small PV equatorward of the core of the westerly jet, steep meridional PV gradients on the polar side of the jet core, and a maximum of PV located off of the pole. In maps of 30 sol mean PV, there is a near-continuous elliptical ring of high PV with roughly constant shape and longitudinal orientation from fall to spring. However, the shape and orientation of the vortex varies on daily time scales, and there is not a continuous ring of PV but rather a series of smaller scale coherent regions of high PV. The PV structure of the Martian polar vortices is, as has been reported before, very different from that of Earth's stratospheric polar vortices, but there are similarities with Earth's tropospheric vortices which also occur at the edge of the Hadley Cell, and have near-uniform small PV equatorward of the jet, and a large increase of PV poleward of the jet due to increased stratification.

1. Introduction

Strong circumpolar winds are observed or inferred in winter middle to high latitudes on Mars, Earth, and several other bodies in the solar system. These so-called polar vortices are important features of an atmosphere's dynamics as well as being important for atmospheric transport. On Mars, the polar vortices may act as a barrier to the transport of dust and ice aerosols toward the winter pole, thus influencing the water cycle and affecting the composition of the seasonal polar cap.

Although temperature observations of Mars have been acquired for many Martian years [e.g., *Smith*, 2008; *Kleinböhl et al.*, 2009], there are no direct measurements of winds in the free atmosphere, which are needed to fully characterize the polar vortices. Insight into the structure of the polar vortices has been obtained from numerical Martian general circulation models (MGCMs) [e.g., *Barnes and Haberle*, 1996] or from inferences of winds from observed temperature [e.g., *Banfield et al.*, 2004; *McConnochie*, 2011]. The recent advent of reanalysis systems for Mars, that combine a general circulation model with observations to produce a best estimate of the atmospheric state, provide new data sets to examine the structure of the polar vortices. *Mitchell et al.* [2015] have recently examined the structure and evolution of the Martian polar vortices and compared with Earth's stratospheric polar vortices using version 1 of the Mars Analysis Correction Data Assimilation (MACDA v1.0) reanalysis [*Montabone et al.*, 2014].

In this work, we revisit the characteristics of the Martian polar vortices using MACDA v1.0 in comparison with output from a preliminary version of the Ensemble Mars Atmosphere Reanalysis System (EMARS) [*Greybush et al.*, 2012]. Considering two reanalysis systems allows us to assess the robustness of these products, e.g., to determine which features are independent of the analysis system used. We examine the potential vorticity structure of the vortices in both reanalyses and examine the seasonal evolution and connections to the meridional circulation (and Hadley Cell). We also compare the polar vortices in the reanalyses with those in free-running versions of the MGCMs used in the reanalysis systems and with polar vortices in Earth's atmosphere.

2. Data

In our analysis we examine the MACDA and EMARS reanalyses, the corresponding free-running Martian general circulation model (MGCM) simulations used in each reanalysis, and temperature retrievals from two satellite instruments. Each of these is described below.

2.1. MACDA

The Mars Analysis Correction Data Assimilation version 1.0 (MACDA v1.0) reanalysis [*Montabone et al*., 2014] spans the period 1999–2004 (which corresponds to the period from late northern summer in Martian year (MY) 24 to late northern spring in MY 27). The MACDA reanalysis uses the Analysis Correction scheme [*Lorenc et al*., 1991] in the UK spectral version of the Laboratoire de Météorologie Dynamique (LMD) MGCM [*Forget et al*., 1999], referred to here as the UK-LMD MGCM (see next paragraph). Observations assimilated into the reanalysis are the retrieved thermal profiles and total dust optical depths from Mars Global Surveyor (MGS) Thermal Emission Spectrometer (TES) infrared nadir atmospheric soundings [*Smith*, 2004]. These retrievals extend from near the surface up to pressures of 0.1 hPa (with vertical resolution of approximately 10 km), so that no data are assimilated at higher altitudes. The MACDA reanalysis has 5° latitude × 5° longitude horizontal resolution and 25 vertical levels (with average pressures between 6.1 hPa and 3.4×10^{-4} hPa).

The UK-LMD MGCM used in MACDA v1.0 has a spectral dynamical core, includes a parameterization for the effects of subgrid scale gravity waves generated by topography [*Forget et al*., 1999], and uses a wideband radiation scheme and visible optical properties for dust from *Clancy and Lee* [1991]. The prescribed column-integrated dust optical depth is derived from the MGS/TES observations, and the vertical distribution of the dust is given by a Conrath profile with parameter z_{max}, that defines the vertical extent of the dust, varying with season and latitude as in *Montmessin et al*. [2004]. The CO_2 microphysics in the model is a simple scheme for condensation and sublimation of CO_2 based on not exceeding saturation. There are no radiatively active water ice clouds in the model.

2.2. EMARS

The preliminary version of the Ensemble Mars Atmosphere Reanalysis System (EMARS) considered here is similar to the "TES dust" version described in *Greybush et al*. [2012]. It assimilates the same MGS/TES temperature profiles as used in MACDA but employs both a different assimilation scheme and GCM. EMARS uses the Local Ensemble Transform Kalman Filter (LETKF) [*Hunt et al*., 2007] for assimilation into the Geophysical Fluid Dynamics Laboratory (GFDL) MGCM [*Wilson and Hamilton*, 1996; *Wilson*, 2011]. The EMARS reanalysis is available for an annual cycle from late northern summer in MY 24 (the start of MGS/TES data), at 5° latitude by 6° longitude resolution and 28 vertical levels up to 3.4×10^{-4} hPa (around 90 km) (i.e., at similar resolution to MACDA).

The version of the GFDL MCGM used for EMARS is described in *Greybush et al*. [2012] and *Zhao et al*. [2015]. This model has a finite volume dynamical core (based on a longitude-latitude coordinate system), includes parameterized topographic gravity wave drag [*Wilson*, 2011], and uses a correlated-k radiation scheme in the infrared radiation where gaseous absorption is relevant (the shortwave heating is calculated in the same fashion as the UK-LMD model). As for the UK-LMD MGCM, the dust optical properties are from *Clancy and Lee* [1991], and there is a simple CO_2 microphysics scheme in the GFDL MGCM. Radiatively active water ice clouds are included. The version of the free-running simulation and EMARS considered here uses a spatially and temporally varying dust optical depth that is very similar to that used in MACDA (the MY 24/25 scenario described in *Montabone et al*. [2015]), but the vertical distribution of dust in the model evolves dynamically as dust (represented by three tracer fields) is advected by the model winds ("TES dust" version of *Greybush et al*. [2012]).

2.3. Satellite Data

We also examine temperatures from the MGS/TES limb-scan retrievals [e.g., *Clancy et al*., 2010; *Guzewich et al*., 2013] and the Mars Reconnaissance Orbiter (MRO) Mars Climate Sounder (MCS) [*Kleinböhl et al*., 2009]. The MGS/TES limb-scan retrievals were not acquired as often as the MGS/TES nadir retrievals and were not assimilated into the MACDA and EMARS reanalyses. These observations extend to higher altitudes than the nadir retrievals. The MRO/MCS retrievals also extend to higher altitudes than the

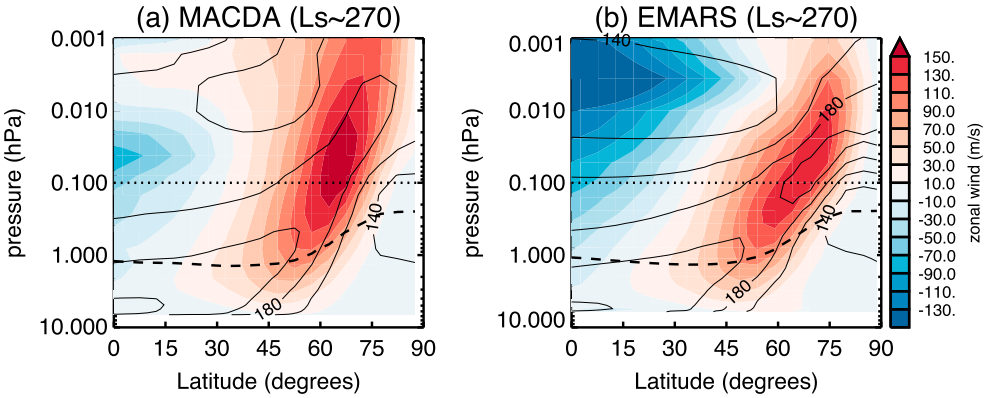

Figure 1. Monthly (30 sol) mean zonal-mean temperature (contours) and zonal-mean zonal wind (shading) as a function of latitude and pressure for $L_s \sim 270°$ for (a) MACDA and (b) EMARS. The dashed curve is the 300 K isentropic surface, and the horizontal dotted line at 0.1 hPa indicates the upper level of the TES data used in the reanalyses.

MGS/TES nadir retrievals but only exist for times after September 2006 (MY 28) and thus do not overlap with the MGS/TES measurements or the reanalyses.

3. Analysis Methodology

The structure of the polar vortices, and related flow, is examined by analyzing temperature, zonal wind velocity, mean meridional circulation, and potential vorticity. Potential vorticity (PV) is defined by

$$\mathrm{PV} = \rho^{-1}\zeta_a \cdot \nabla\theta,$$

where ρ is the fluid density, $\boldsymbol{\zeta}_a$ is the absolute vorticity, and $\nabla\theta$ is the gradient of the potential temperature. Potential vorticity is useful for studying polar vortices because (i) PV is materially conserved for adiabatic, frictionless flows, (ii) other dynamical fields can be determined using "PV inversion," and (iii) PV gradients provide the restoring mechanism for Rossby waves, so that the dynamics and propagation of these waves is best understood by examining the distribution of PV [e.g., *Hoskins et al*., 1985]. Since both PV and potential temperature (θ) are materially conserved for adiabatic and frictionless flows, analysis of PV is most often performed on isentropic surfaces (surfaces of constant θ). The magnitude of PV can increase rapidly with altitude, due primarily to the $1/\rho$ factor, and thus *Lait* [1994] introduced a scaled PV

$$\mathrm{PV}_s = \mathrm{PV}(\theta/\theta_0)^{-(1\ +\ cp/R)},$$

where θ_0 is an arbitrarily chosen potential temperature reference level (we have chosen $\theta_0 = 200$ K, as used in *Mitchell et al*. [2015]), and c_p/R is the ratio of specific heat at constant pressure to the universal gas constant ($c_p/R = 4.0$ for Mars). (Note that this value of c_p/R differs from the value of 4.4 used in *Mitchell et al*. [2015]. We use $c_p/R = 4.0$ to be consistent with the value used in the free-running models.) The $\theta^{-(1\ +\ cp/R)}$ term removes much of the vertical variation of PV in an isothermal atmosphere.

In our analysis, we focus on reanalyses covering the first Martian annual cycle measured by TES, beginning at solar longitude (L_s) 141° in MY 24, i.e., we consider the period MY 24 $L_s = 141°$ to MY 25 $L_s = 140°$. In much of our analysis we examine fields averaged over 30 Martian sols, with the first 30 sol average covering MY 24 L_s 141°–157° and the second covering MY 24 L_s 157°–174° (these 30 sol averages correspond to the periods covered by each data file for MACDA v1.0). To enable consistent comparison between the differing vertical resolution of the reanalyses, models, and observational data, we interpolate all fields on to the same 13 pressure levels between 5 hPa and 0.005 hPa.

4. Zonal-Mean Fields

4.1. Temperature and Zonal Winds

4.1.1. Comparison of Reanalyses

We first consider the zonal-mean temperature (T) and zonal wind (U) during Northern Hemisphere (NH) winter, focusing on middle and high latitudes. Figure 1 shows the latitudinal-pressure variation of

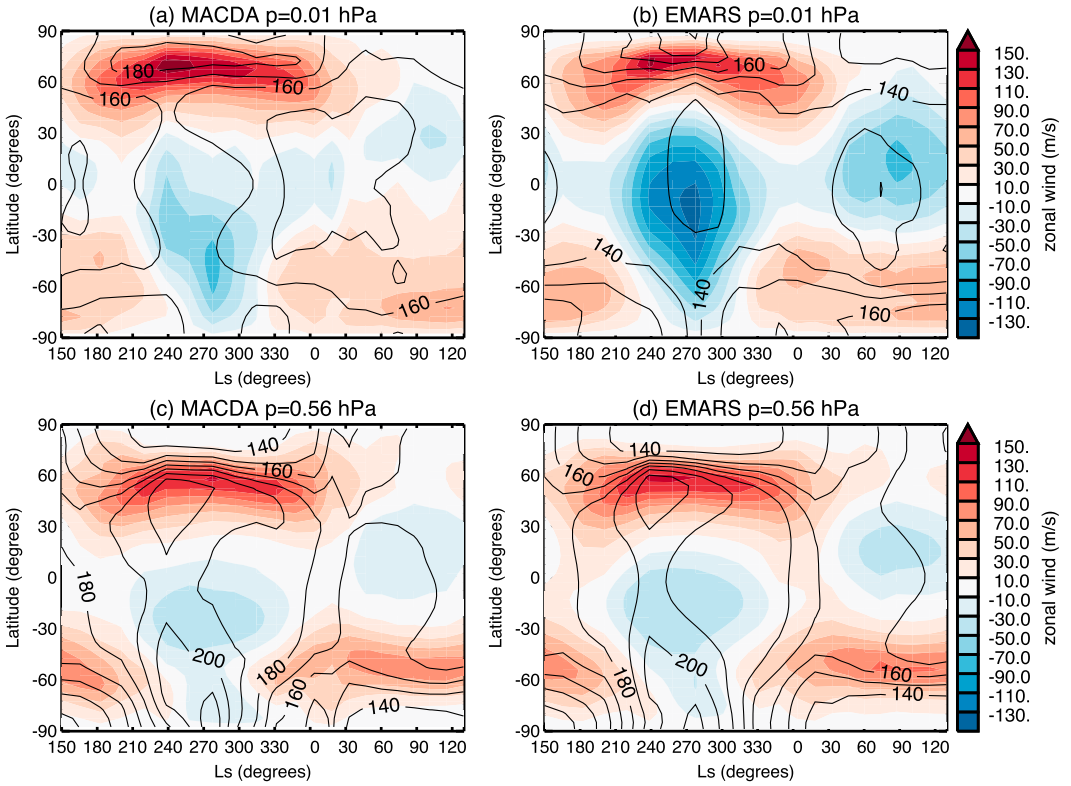

Figure 2. Zonal-mean temperature (contours) and zonal-mean zonal wind (shading) as a function of latitude and season on the (a, b) 0.01 hPa and (c, d) 0.56 hPa surfaces, for MACDA (Figures 2a and 2c) and EMARS (Figures 2b and 2d).

monthly-mean zonal-mean T and U around the northern winter solstice ($L_s = 270°$), for MACDA and EMARS. Both reanalyses show strong westerly winds (exceeding 150 m/s) in winter high latitudes, coincident with a large meridional temperature gradient and low polar air temperatures (below 140 K). The winter "polar jet" tilts toward the pole with height, with maximum winds at each level occurring around 50°N at 5 hPa but occurring poleward of 70°N above 0.01 hPa. In the upper atmosphere (pressure around 0.01 hPa) there is a reversal of the meridional temperature gradient with higher temperatures occurring at the north pole, corresponding to the so-called "polar warming" [e.g., *McDunn et al.*, 2013].

There is very good agreement between the two reanalyses in the lower atmosphere where TES data are assimilated (pressures greater than 0.1 hPa), with similar meridional temperature gradients and maximum westerlies. However, there are differences in the upper atmosphere (pressures less than 0.1 hPa), with the westerlies confined to higher latitudes in EMARS compared with MACDA, as well as lower tropical temperatures and stronger tropical easterlies in EMARS. As discussed below, the differences between MACDA and EMARS at pressures less than 0.1 hPa are related to differences in the MGCM simulations used in each reanalysis.

The agreement between reanalyses in the lower atmosphere holds throughout the year, as shown in Figures 2c and 2d. In both reanalyses low polar temperatures and strong westerlies in the Northern Hemisphere develop in early autumn ($L_s = 180°$) and persist until spring ($L_s = 0°$), with approximately consistent maximum winds (and minimum temperatures) from $L_s \sim 210°$–$320°$. There is a similar seasonal evolution in the winter for the Southern Hemisphere (SH), but the westerly jet is weaker than that during the winter in the NH. The winter polar temperatures are similar between hemispheres (because CO_2 condensation provides a lower limit on the temperature), and from this, it may be expected that the jet strengths would be similar. However, the SH winter middle latitude temperatures are lower than the NH winter middle latitude temperatures, and this results in weaker meridional temperature gradients and an overall weaker jet in the SH.

The seasonal evolution of temperatures and winds in the upper atmosphere differs between the reanalyses; see Figures 2a and 2b. In MACDA the polar temperatures and zonal winds at 0.01 hPa are of roughly constant

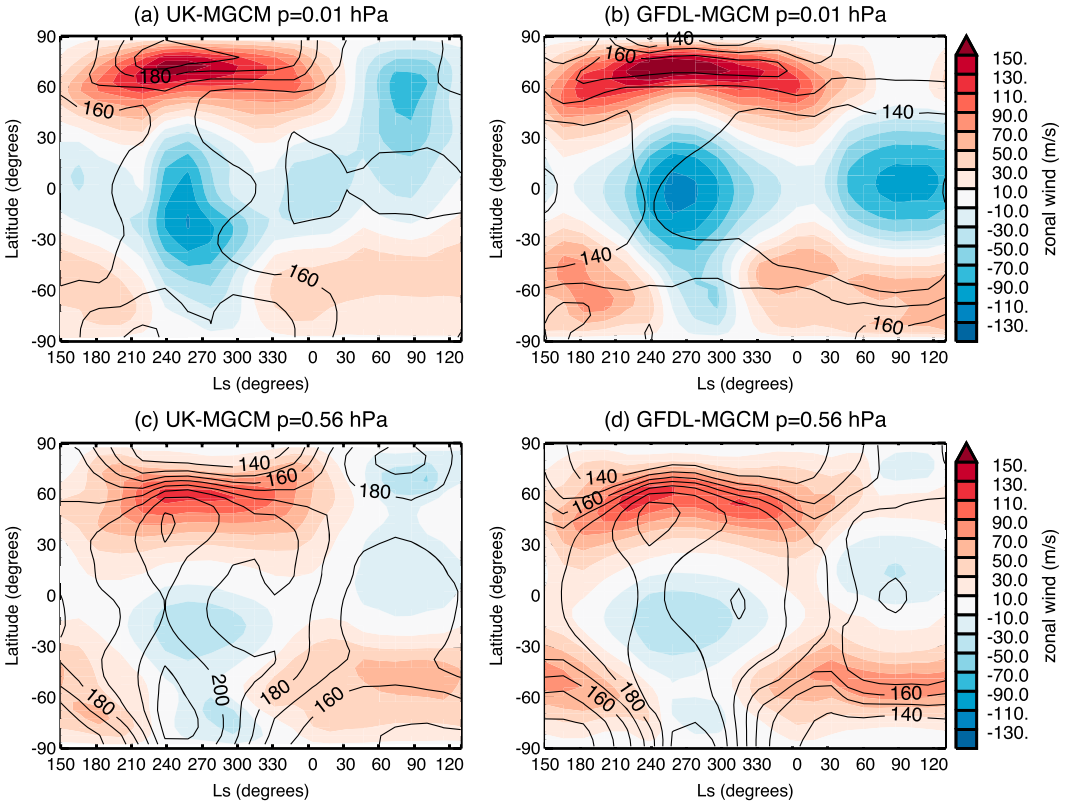

Figure 3. Zonal-mean temperature (contours) and zonal-mean zonal wind (shading) as a function of latitude and season on the (a, b) 0.01 hPa and (c, d) 0.56 hPa surfaces, for UK-MGCM (Figures 3a and 3c) and GFDL-MGCM (Figures 3b and Figure 3d).

strength through Northern Hemisphere autumn and winter ($L_s = 180°$ to $L_s = 0°$), but EMARS shows a weakening of the westerly jet and polar warming around the NH winter solstice that is not found in MACDA. There are also differences between the reanalyses at low latitudes and in southern high latitudes: There are stronger tropical easterlies during both northern and southern winters, and stronger middle latitude westerlies during southern winter, in EMARS.

We have focused here on the first Martian annual cycle in the reanalyses, as only this period is available for EMARS. However, analysis of the multiyear MACDA record shows small interannual variability in the polar temperatures and jet strength [e.g., see *Mitchell et al.*, 2015, Figure 7] and the general features discussed above hold for all years in the MACDA record.

4.1.2. Comparison With Free-Running GCMs

To understand the above differences between the reanalyses we examine output from the free-running MGCMs on which the reanalysis systems are based. Figure 3 show the seasonal evolution of the zonal-mean temperature and zonal wind at (a, b) 0.01 hPa and (c, d) 0.56 hPa, from the UK-LMD and GFDL MGCMs (and can be compared with reanalyses in Figure 2). There are some substantial differences between the two free-running simulations, in both the lower and upper atmospheres. The low north polar temperatures and strong westerlies around 60°N form earlier and persist longer into summer in the GFDL simulation, and there is a polar warming and weakening of the westerly jet around $L_s = 270°$ in the GFDL model that is not in the UK-LMD model. There are also differences in the tropics and SH, with stronger tropical easterlies and SH winter westerlies in the GFDL model.

The differences between the free-running models in the upper atmosphere (where MGS/TES data are not assimilated; altitudes above 0.1 hPa) are similar to the differences between the reanalyses (compare Figures 3a and 3b with Figures 2a and 2b; see also Figure 4 below). In fact, the fields at 0.01 hPa from each free-running model are generally more similar to their corresponding reanalysis than to those fields in the other free-running model or reanalysis. The similarity between free-running model simulation and reanalysis indicates that the MGCM simulations exert a strong influence on the (unconstrained) reanalysis at this level.

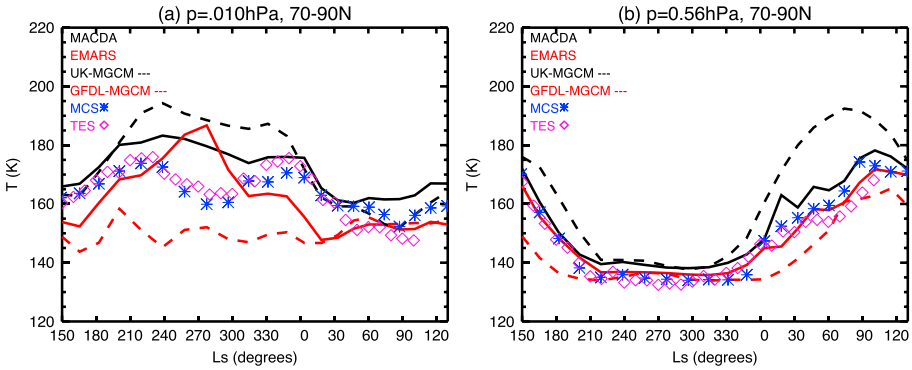

Figure 4. Seasonal evolution of the 70–90°N average temperature on the (a) 0.01 hPa and (b) 0.56 hPa surfaces. See text for details.

The conclusions regarding the role of the MGCM in differences between the reanalyses are however different at altitudes where MGS/TES data are assimilated (altitudes below 0.1 hPa). Here differences between the free-running models do not drive commensurate differences in the reanalyses, and the difference between the two reanalyses are generally smaller than the differences between each reanalysis and its corresponding free-running simulation. This close agreement in reanalyses, in spite of differences in the underlying free-running model simulations, indicates that the reanalyses in the lower atmosphere are controlled by the assimilated data and not the underlying MGCM.

Although examining the free-running simulations is not the main focus of this study, it is of interest to speculate on why there are large differences, especially in the upper atmosphere. The UK-LMD and GFDL simulations examined above have many common features (e.g., inclusion of topographic wave drag and damping in the upper levels, and use of the same, or very similar, horizontal distribution and optical properties for dust), but there are some differences. The models have different dynamical cores, i.e., use different numerical methods to solve the dynamical equations (UK-LMD uses a spectral method, while GFDL uses a finite volume method on a regular latitude-longitude grid), the vertical distributions of dust differs, and only the GFDL model includes radiatively active water-ice clouds. Previous studies have shown that the simulated upper atmosphere is very sensitive to these aspects. For example, *Forget et al.* [1999] compared simulations between two models with identical physics and aerosol distributions but different dynamical cores (grid point or spectral) and showed that there are large differences in the upper atmosphere. They concluded that Mars middle atmosphere above 40 km is very model sensitive and difficult to simulate accurately. Also, the modeling studies of *Madeleine et al.* [2011] and *Guzewich et al.* [2013, 2016] show that the simulated flow is very sensitive to the distribution of dust within the model, especially during northern winter. Finally, studies have shown that inclusion of radiatively active water ice clouds has a substantial influence on the simulated temperature structure [e.g., *Madeleine et al.*, 2012; *Wilson et al.*, 2008, *Wilson and Guzewich*, 2014]. Additional simulations with the GFDL model using different dynamical cores (finite volume and spectral) or differing dust distributions also show large sensitivity in the upper atmosphere (not shown). Given the above studies (and the additional sensitivity simulations with the GFDL model), it is not surprising that there are some substantial differences between the UK-LMD and GFDL simulations. Further analysis of the free-running simulations and comparisons with observations is required to improve the representation of the atmosphere in these models and in the reanalyses but is beyond the scope of this paper.

4.1.3. Comparison With Observations

Given the differences between the two reanalyses in the upper atmosphere where TES data are not assimilated, an obvious question is which reanalysis most closely corresponds to actual conditions. Fortunately, we have access to TES limb-scan and MCS temperature retrievals to conduct a comparison in this region of the atmosphere. The TES limb-scan observations are for the same period but were not used in the data assimilation in either reanalysis, whereas the MCS observations are for later years (MY 28 to present). We include the MCS data for comparison because there is limited interannual variability in temperatures outside of time periods with large dust storms [*Shirley et al.*, 2015; *Guzewich et al.*, 2016].

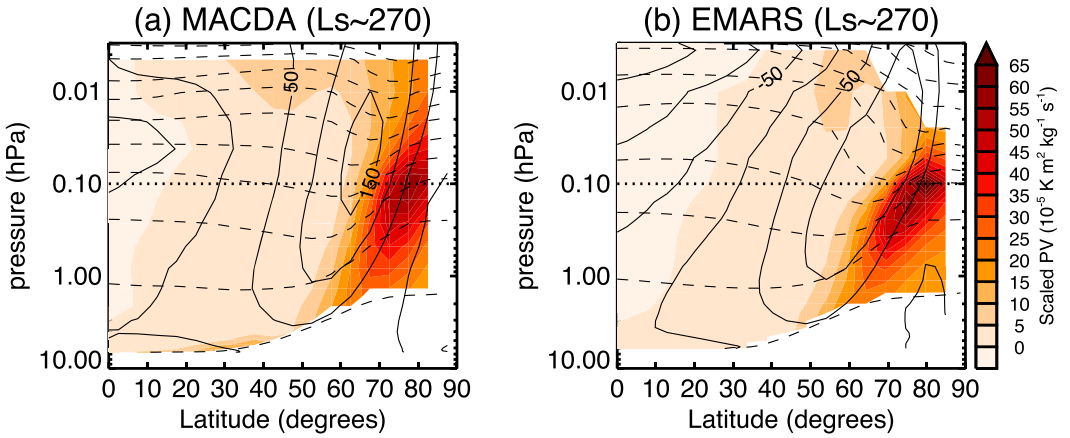

Figure 5. Monthly-mean zonal-mean scaled potential vorticity (shading), zonal wind (solid contours), and potential temperature (dashed contours, corresponding to 250, 300, … K) as a function of latitude and pressure for $L_s \sim 270°$ for (a) MACDA and (b) EMARS. The horizontal dotted line at 0.1 hPa indicates the upper level of the TES data used in the reanalyses.

In Figure 4 we compare the reanalysis temperatures with those from TES limb-scan and MCS measurements. The solid curves show the seasonal evolution of the 70–90°N average temperature from the two reanalyzes, while the symbols show temperatures from TES limb-scan data for MY 24 and 25 and MCS data for MY 29 to 32 (data for MY 28 are not used as during this year there was a large dust storm that disturbed the northern polar vortex [*Guzewich et al*., 2016]). At both levels there is good agreement between the two observational data sets.

At 0.56 hPa there is also good agreement between the reanalyses and the observations, with EMARS matching the observations very closely and MACDA having a small warm bias. As discussed above, the two reanalyses generally agree better than either reanalysis with its corresponding free-running MGCM (dashed curves), especially in nonwinter seasons. This highlights the strong influence of the data in constraining the reanalyses in the lower atmosphere. There is, however, less agreement at the 0.01 hPa level. At this level MACDA is warmer than the observations, while EMARS is colder than observations except around the winter solstice ($L_s \sim 270^o$). Similar signed biases exist between the corresponding free-running MGCMs and the observations, showing the dominant influence of the MGCM simulations on the reanalysis at this level.

Similar comparisons for the SH show similar results with good agreement between both reanalyses and observations in the lower atmosphere but differences between reanalyses and observations in the upper atmosphere (not shown).

4.2. Potential Vorticity

We now consider the polar vortex from the potential vorticity (PV) perspective. As discussed in section 3, PV has several useful properties for understanding vortex dynamics and the propagation of Rossby waves.

In both reanalyses the area of high PV is confined to the northern polar region, with low PV at and equatorward of the polar jet maximum, see, for example, Figure 5 which shows the latitudinal-pressure variation of monthly-mean zonal-mean scaled potential vorticity (PV_S, see section 3) calculated for each reanalysis, for the NH winter solstice. Figure 5 also shows, as discussed in *Mitchell et al*. [2015] for MACDA, that the maximum value of PV occurs off of the pole in the lower atmosphere. This feature was also shown in earlier modeling [*Barnes and Haberle*, 1996] and observational [*Banfield et al*., 2004; *McConnochie*, 2011] studies. Another notable feature is that there are weak PV gradients at the jet maximum, and the steepest PV gradients are on the poleward side of the jet. This difference in latitude of maximum zonal winds and latitude of maximum PV gradients means that the "size" of the polar vortex will depend on whether its extent is defined using PV or zonal winds, i.e., the vortex will be smaller if defined by maximum PV gradients (as in *Mitchell et al*. [2015]) compared to a definition based on maximum zonal winds.

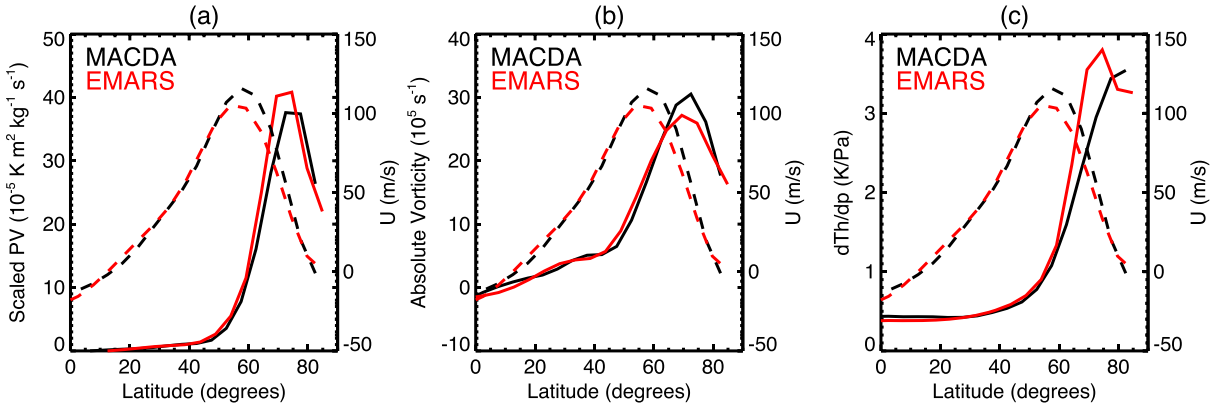

Figure 6. Variation of monthly-mean zonal-mean (a) scaled EPV, (b) absolute vorticity, and (c) $d\theta/dp$ as a function of latitude for the $\theta = 300$ K isentropic surface at $L_s \sim 270°$ for MACDA (black) and EMARS (red). The monthly-mean zonal-mean zonal wind is also shown with dashed lines.

The different latitudes of the maximum zonal wind and maximum PV gradient are highlighted in Figure 6, where the latitudinal variations of zonal-mean U and PV at 300 K are shown. An approximate equation for PV, valid for large Richardson number, is [*Clough et al.*, 1985]

$$PV \sim g\zeta_{a,v}|d\theta/dp|,$$

where $\zeta_{a,v}$ is the vertical (perpendicular to the constant pressure surface) component of absolute vorticity and Figures 6 also shows the latitudinal variations of $\zeta_{a,v}$ and $d\theta/dp$. The PV, $\zeta_{a,v}$, and $d\theta/dp$ all have qualitatively similar latitudinal structure, except at very high latitude. There are very weak meridional gradients and small values in all quantities in low and middle latitudes, with a rapid increase (large meridional gradients) around or north of the maximum zonal-mean winds (jet core). There are quantitative differences between quantities, with the maximum meridional gradient in $\zeta_{a,v}$ roughly colocated with the jet core, while the largest increase in $d\theta/dp$ occurs north of the jet. Also, especially for MACDA, the peak $d\theta/dp$ occurs north of the peak of $\zeta_{a,v}$. As PV is proportional to the product of $\zeta_{a,v}$ and $d\theta/dp$, the small values of both quantities south of the jet (relative to high latitudes) results in the very low PV for these latitudes. Poleward of the jet, PV increases rapidly with latitude because of increases in $\zeta_{a,v}$ and $d\theta/dp$ and peaks at a similar latitude to the peak $\zeta_{a,v}$.

The seasonal evolution of the polar PV in the lower atmosphere is similar to that of the westerly jet (Figure 7), with large PV developing in early autumn ($L_s = 180°$ in the NH) and persisting until spring ($L_s = 0°$ in the NH). The PV structure and evolution is similar in the two hemispheres, although the maximum PV in the SH is weaker than in the NH (consistent with the differences in zonal winds), and the maximum PV occurs closer to the pole.

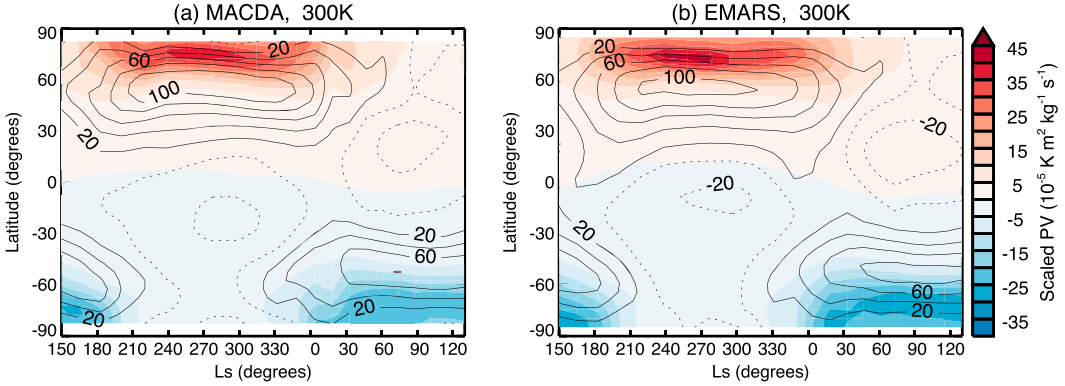

Figure 7. Zonal-mean scaled potential vorticity (shading) and zonal-mean zonal wind (contours) as a function of latitude and season on the $\theta = 300$ K isentropic surface for (a) MACDA and (b) EMARS.

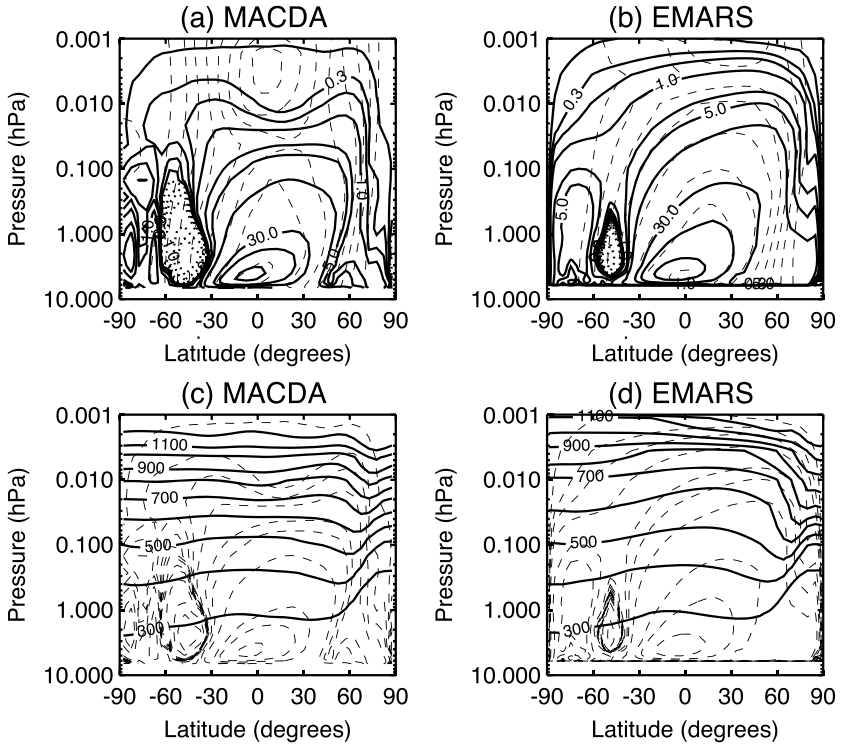

Figure 8. (a, b) Mean meridional circulation (solid contours; 10^8 kg/s) and angular momentum (dashed contours; 10^8 m^2/s) and (c, d) zonal-mean potential temperature (solid contours corresponding to 300, 400, … K) mean meridional circulation (dashed contours) as a function of latitude and pressure for $L_s \sim 270°$ for MACDA (Figures 8a and 8c) and EMARS (Figures 8b and 8d).

4.3. Mean Meridional Circulation

Several of the characteristics of the polar vortices, as well as differences between reanalyses, can be related to the mean meridional circulation. As shown in Figures 8a and 8b, at the NH winter solstice the mean meridional circulation consists of a single near-global overturning cell with air ascending in southern middle latitudes and descending in northern high latitudes. The characteristics of this so-called "Hadley Cell" (HC) are similar to that in previous MGCM simulations [e.g., *Barnes and Haberle*, 1996; *Wilson*, 1997; *Forget et al*., 1999]. Again similar to these previous studies, in both reanalyses contours of angular momentum ($M = ua\cos\varphi + \Omega a^2\cos^2\varphi$, where a is the planetary radius, Ω is the planetary rotation rate, and φ is latitude) are close to parallel to the meridional stream function throughout much of the low and middle latitudes (compare dashed and solid curves in Figures 8a and 8b). In other words, the summer-to-winter meridional circulation is close to being angular momentum conserving.

The latitudinal variations in absolute vorticity and stratification ($d\theta/dp$) discussed in the previous section are closely coupled to the near-global HC. Consistent with theoretical expectations for near-inviscid HCs [e.g., *Held and Hou*, 1980], there is a rapid increase in zonal winds (i.e., the jet core) north of the HC (region with angular momentum conserving meridional circulation), e.g., compare Figures 1 and 8. This produces the latitudinal variation of zonal winds and absolute vorticity shown in Figure 6. Also consistent with theory, there are very weak meridional gradients of θ and near-uniform $d\theta/dp$ within the HC (solid curves in Figures 8c and 8d). Poleward of this there is a rapid increase in θ and $d\theta/dp$ because of adiabatic warming in the descending air [e.g., *Wilson*, 1997]. As discussed above, the small values of absolute vorticity and $d\theta/dp$ in low and middle latitudes (within the near-inviscid HC) compared to values at high latitudes results in relatively small PV equatorward of the jet core.

There are again some quantitative differences between the reanalyses. The mean meridional circulation in EMARS is stronger and extends further into the upper atmosphere than in MACDA. This stronger/broader HC in EMARS results in stronger polar descent and depression of polar isentropes (adiabatic warming of polar air) in EMARS.

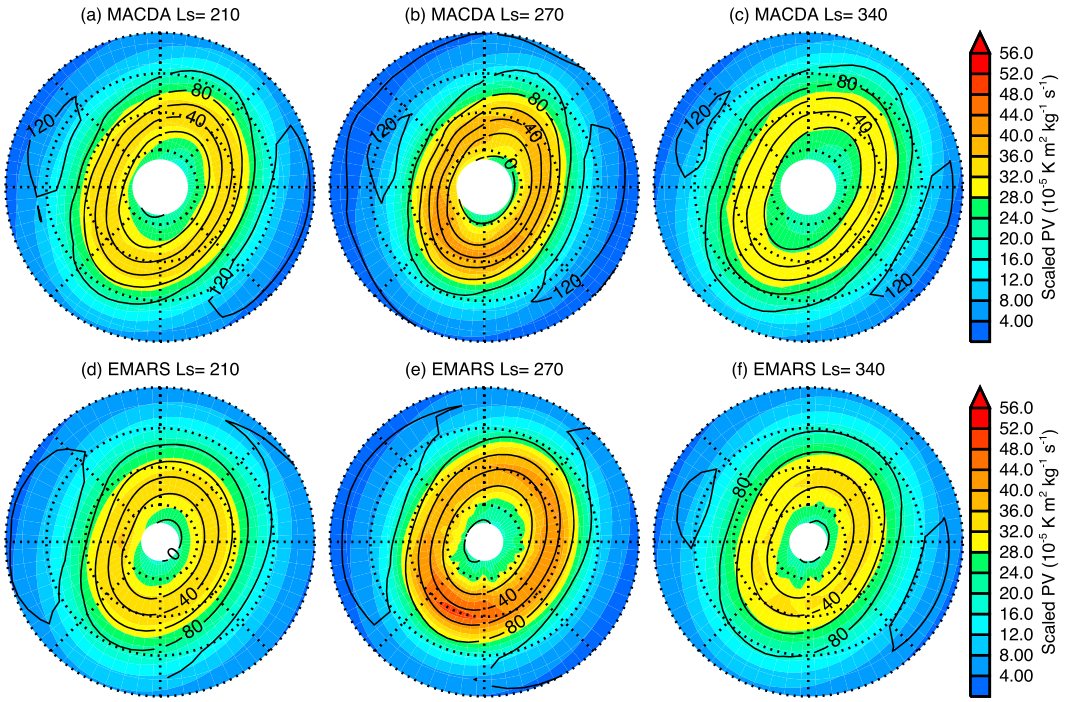

Figure 9. North polar stereographic projection maps of monthly-mean PV (shading) and zonal winds (contours) on the $\theta = 300$ K isentropic surface for (a, d) $L_s \sim 210°$, (b, e) $L_s \sim 270°$, and (c, f) $L_s \sim 340°$, for MACDA (Figures 9a–9c) and EMARS (Figures 9d–9f). The outer latitude is 50°N and 0° longitude is at the bottom of the maps.

During southern winter the meridional circulation is weaker, shallower, and less global in extent (not shown). This is due primarily to the north-south topographic dichotomy (i.e., higher average topography in the Southern Hemisphere) on Mars [e.g., *Richardson and Wilson*, 2002; *Zalucha et al.*, 2010], although differences in the aerosol forcing between the two solsticial periods likely also contribute to differences in the circulation [e.g., *Basu et al.*, 2006]. Consistent with the above discussion, there is weaker polar descent and adiabatic warming in southern high latitudes during SH winter (not shown).

5. Horizontal Structure

The above analysis has focused on the monthly-mean zonal-mean structure of the vortices but to more fully understand the dynamics of the vortices we need to additionally consider both longitudinal variations and the evolution on shorter time scales.

Considering longitudinal variations first, Figure 9 shows maps of the 30 sol mean zonal winds and PV on the $\theta = 300$ K isentropic surface (in the lower atmosphere where TES nadir data has been assimilated) for mid-autumn ($L_s \sim 210°$), winter solstice ($L_s \sim 270°$), and late winter ($L_s \sim 340°$). Several features already discussed above can be clearly seen in these maps: uniform, low PV in middle and low latitudes; maximum PV gradients poleward of the maximum zonal winds; and latitude of maximum PV displaced off of the pole. In addition, the maps show that the region of high PV forms an elliptical annulus, with major axis aligned close to 30°W–150°E, that is centered close to the pole. The orientation of the vortex is consistent with previous studies documenting stationary zonal wave number 2 waves in the Martian atmosphere [e.g., *Banfield et al.*, 2003]. The magnitude of the PV varies through autumn and winter (with maximum values around the solstice), but the size and orientation of the PV annulus is fairly constant. The vortex has similar shape and orientation in the two reanalyses, although the EMARS vortex is slightly more circular than the MACDA vortex. *Mitchell et al.* [2015] present a more detailed analysis of the shape and vertical variations of the polar vortices in MACDA.

The structure and agreement between reanalyses is somewhat different for the SH vortex, as can be seen in Figure 10, which shows maps of the 30 sol mean zonal winds and PV in the Southern Hemisphere for mid-

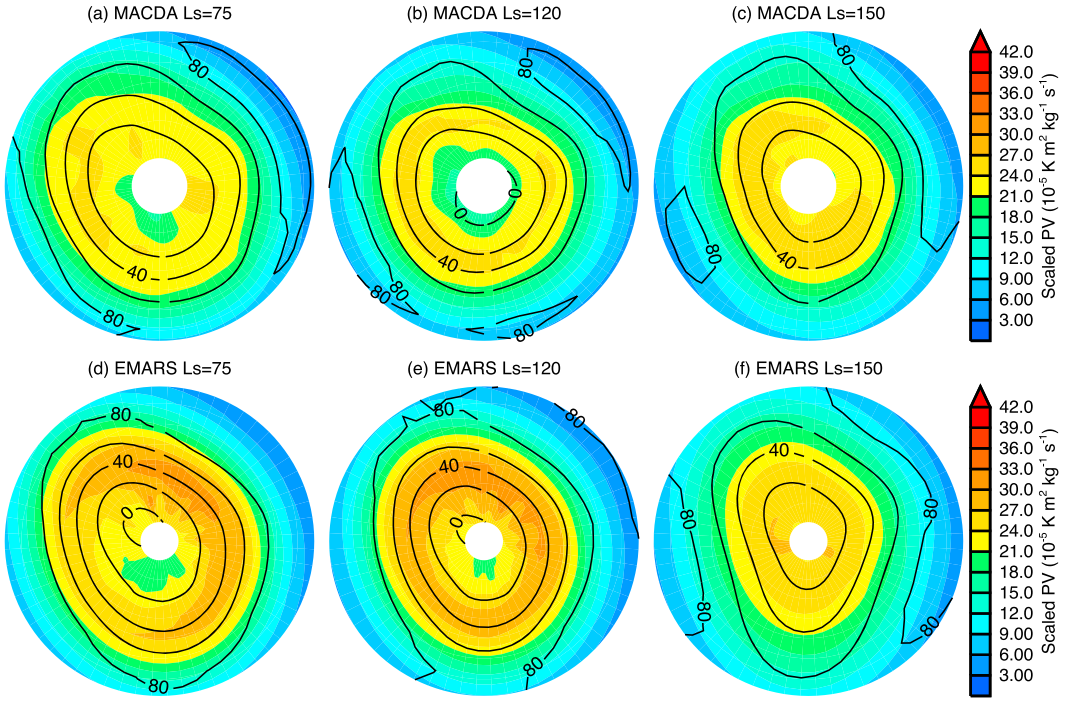

Figure 10. Same as Figure 9 except showing Southern Hemisphere projection for (a, d) $L_s \sim 75°$, (b, e) $L_s \sim 120°$, and (c, f) $L_s \sim 150°$.

autumn ($L_s \sim 75°$), winter solstice ($L_s \sim 120°$), and late winter ($L_s \sim 150°$). The SH vortex has lower PV and is less elliptical than in the NH, and there are larger differences between the reanalyses. EMARS shows a clear annulus between mid-autumn to late winter, whereas there is a weak annulus only in mid-autumn to winter solstice in MACDA.

An important question is whether the PV annulus is a real feature of the Martian atmosphere or an artifact of the reanalyses. To start to address this issue we examine the spatial distribution of PV in the free-running MGCMs as well. Figure 11 shows NH 30 sol mean PV and U for the UK-LMD and GFDL MGCMs for same periods shown in Figure 9. There are some substantial differences in the PV structure from each MGCMs and the corresponding reanalysis, as well as differences between the MGCMs.

The size of the vortex in the UK-LMD MGCM is smaller than in the reanalyses (equivalently, there is a weaker jet and weaker meridional gradients of the zonal winds in the UK-LMD MGCM), and it is unclear if the region of high PV is an annulus. (We have not calculated PV at the most poleward grid point, but if one-sided differences are used to approximate the latitudinal derivatives in the PV calculation at these latitudes, there are slight indications of an off-polar latitude of maximum PV; e.g., see *Mitchell et al.* [2015].) This implies that the annulus with high PV values that peak well away from the pole in MACDA comes from the assimilation of the TES temperature data.

The picture for the GFDL simulation is different. There is a clear annulus of high PV in early autumn and late winter, with similar size but slightly different orientation than in the EMARS reanalysis. This shows that free-running MGCMs can generate a PV annulus and suggests that the PV annuli in the reanalyses are not an artifact of the assimilation process. At winter solstice there is a weak vortex in the GFDL model, due to the transient midwinter polar warming which disrupts the vortex at all altitudes. The transient polar warming is highly dependent on the aerosol distribution (amount and vertical extent) used in the free-running simulation. See *Guzewich et al.* [2016] for further discussion of transient warmings in MarsWRF simulations and dependence on aerosol distribution. Even though there is polar warming in the free-running simulation, the assimilation of TES observations results in the maintenance of a strong vortex and PV annulus throughout the winter in EMARS.

The analysis above has focused on vortex structure in 30 sol mean fields. We have also examined the instantaneous and daily average PV fields, and these show some differences in vortex structure. Whereas the 30 sol

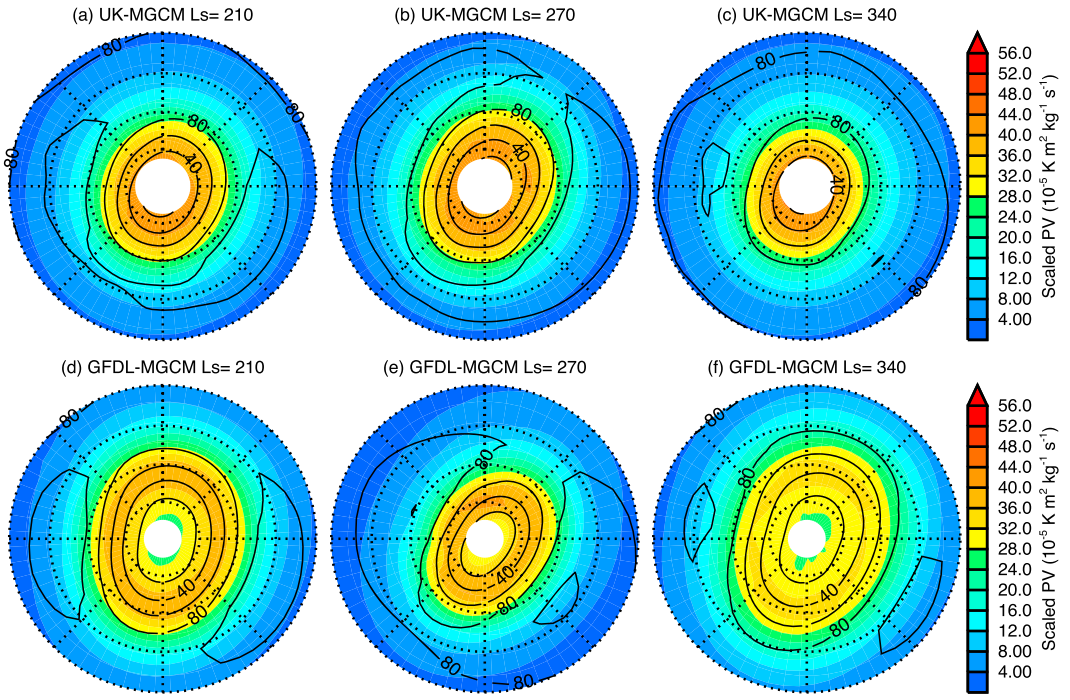

Figure 11. Same as Figure 9 except showing identical fields from the (a–c) UK-LMD and (d–f) GFDL MGCMs.

mean fields show a continuous, nearly elliptical, annulus of high PV with similar orientation throughout winter, the shape and orientation of the vortex varies on daily time scales and there are also smaller-scale coherent regions of high PV in the instantaneous PV. This is illustrated in Figure 12 which shows maps of instantaneous PV for each reanalysis for three consecutive sols at $L_s = 216^o$, for MACDA and EMARS. The exact shape of the vortex and location/structure of the small-scale high PV regions differs between the reanalyses, but for both reanalyses these features rotate around the pole and are observed throughout the winter. It is only when averaged over monthly time scales that these "blobs" of high PV appear as a near-continuous elliptical ring (as in Figure 9).

Again an important question is whether these features in the instantaneous PV are real. As discussed above, PV annuli are found in the GFDL free simulation. The instantaneous PV in the GFDL model also shows variable shape and orientation of the vortex and small-scale high-PV regions (e.g., Figure 12c). However, the shape is less variable and the small-scale high-PV features are more elongated than in the reanalyses. Preliminary analysis of higher resolution GFDL model simulations [*Wilson*, 2011] as well as MarsWRF simulations [*Guzewich et al*., 2016] also shows small-scale regions of high PV within the annulus that are more elongated and less like the "blobs" in the reanalyses. This suggests that the blobs in the reanalyses PV may in part be due to the assimilation process or (insufficient) resolution.

Although there is some uncertainty regarding the reality of the small-scale PV blobs, there is a fluid dynamical reason to expect such features. An annular vortex has opposite-signed PV gradients either side of the peak PV and satisfies the necessary condition for barotropic instability. This does not mean the vortex is definitely unstable, but linear stability analysis of barotropic flow on a sphere by *Hartmann* [1983] and *Dritschel and Polvani* [1992] shows that flows with similar vorticity structure to the Martian vortices are linearly unstable. Furthermore, numerical simulations indicate that this instability leads to a breakup of the annulus into a ring of small-scale vortices [e.g., *Dritschel and Polvani*, 1992; *Ishioka and Yoden*, 1994]. It is therefore possible that the PV blobs in the Martian reanalyses are the result of barotropic instability. In the above idealized barotropic simulations the small-scale vortices often coalesce together, eventually forming a single monopolar vortex. This does not occur in the reanalyses, perhaps because additional diabatic processes (including latent heating due to condensation of CO_2) oppose the instability and maintain the annular vortex. We are currently performing modeling experiments to examine the possible role of barotropic instability and the balance between this instability and diabatic processes.

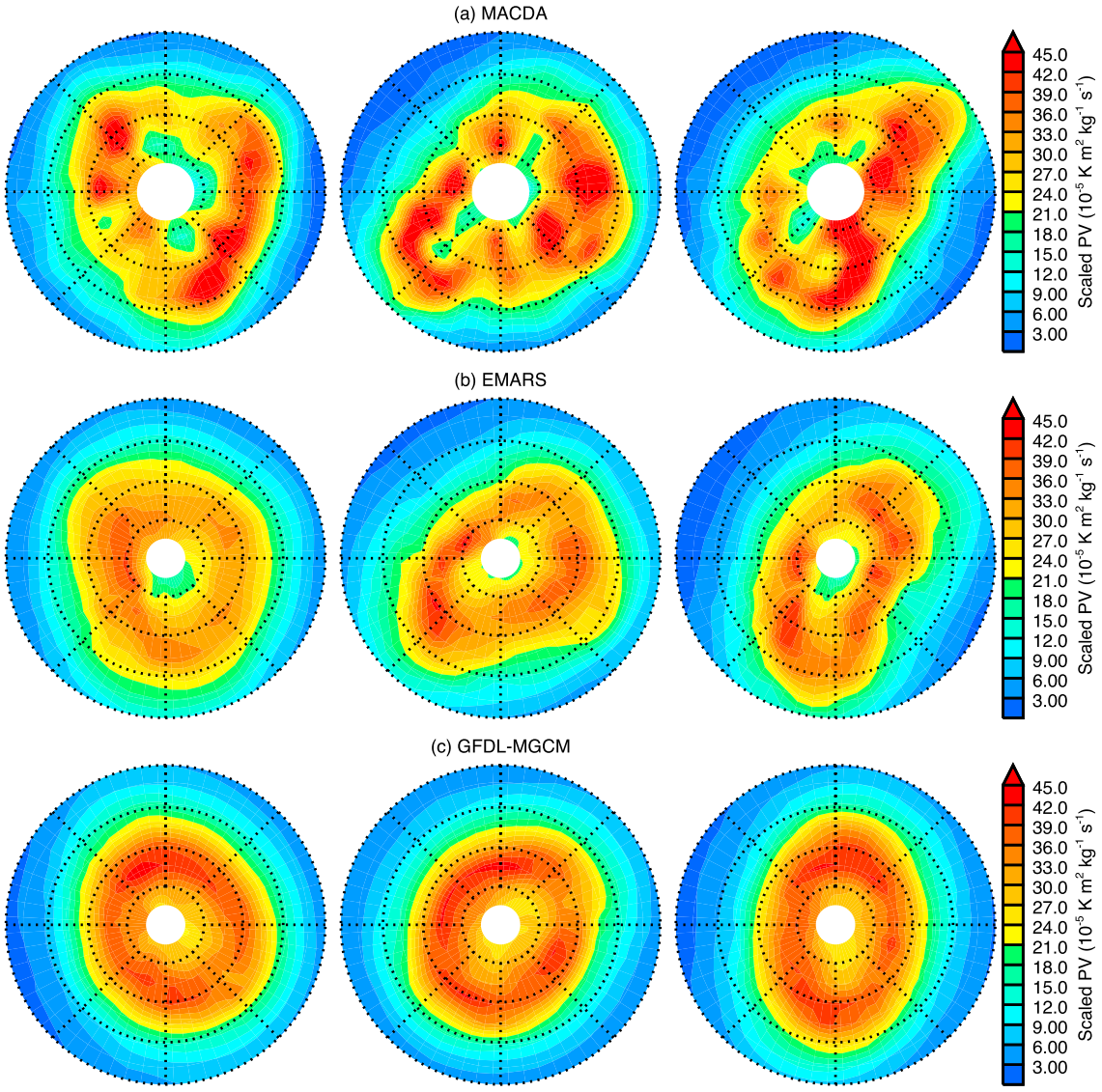

Figure 12. North polar stereographic projection maps of instantaneous PV at $L_s = 216°$ on the $\theta = 300$ K isentropic surface for (a) MACDA, (b) EMARS, and (c) GFDL-MGCM. For each reanalysis the maps are 1 sol apart, and the same Mars universal time (MUT) is shown for reanalyses and the model.

6. Comparison With Earth

Finally, we compare the polar vortices on Mars with those on Earth. In Earth's atmosphere there are distinct stratospheric and tropospheric polar vortices [*Waugh et al.*, 2016]; see Figure 13. *Mitchell et al.* [2015] compared Martian polar vortices with those in the Earth's stratosphere and showed that while in both cases there is a strong westerly jet at middle to high latitudes, with high PV poleward of the jet, there are several differences: the NH winter vortex is stronger than its SH winter counterpart on Mars, while the reverse is true on Earth; Martian polar vortices exhibit less variability than Earth's stratospheric vortices; and there is a ring of high PV, with a peak in latitude offset from the pole, in the lower atmosphere of Mars, whereas in Earth's stratosphere there is generally a circular and monotonic PV distribution with highest values at the center (Figure 14a). Another difference (not discussed in *Mitchell et al.* [2015]) is that in Earth's stratosphere there are large PV gradients in the middle latitudes and the maximum PV gradients are generally colocated with the jet core (Figure 14a), whereas, as discussed above, on Mars, there is very low PV at and equatorward of the jet core and the maximum PV gradients are poleward of the jet core. This difference in the relative location of maximum winds and maximum PV gradients is related to differences in $d\theta/dp$: on Mars there is

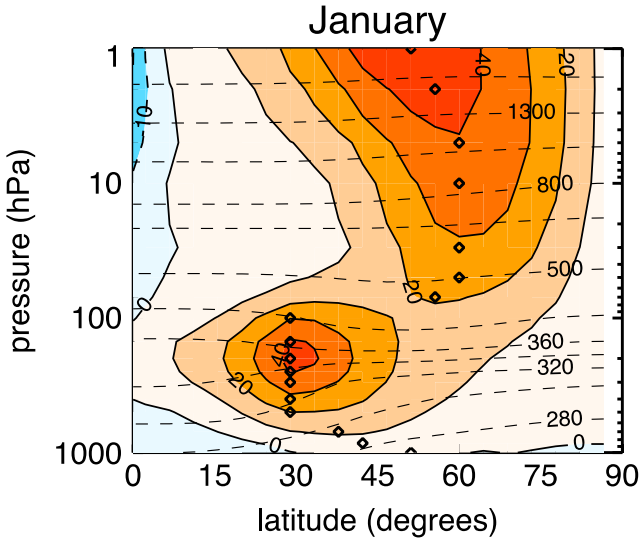

Figure 13. Climatological January mean zonal-mean zonal winds (shading and sold contours) and potential temperature (dashed contours) as a function of latitude and pressure for the Earth's atmosphere. The diamond symbols mark the hemispheric maximum of the zonal wind at each pressure level and thus the approximate edge of the polar vortex.

a large increase in dθ/dp poleward of the jet (Figure 4), but this is not the case in Earth's stratosphere where isentropes are close to parallel with the isobars and dθ/dp varies little with latitude (Figure 14a).

Most of the differences enumerated above can be linked to fact that the Martian polar vortices are being compared with the stratospheric polar vortices on Earth. As discussed above, the Martian polar vortices are directly connected with the Hadley Cell (HC), e.g., the vortices occur at the edge of the HC, there is low PV inside the HC, and there is strong descent on the poleward edge of HC. However, there is no direct connection between the Hadley Cell and stratospheric polar vortices in Earth's atmosphere, and the stratospheric polar vortex does not depend on HC dynamics.

Rather than just merely compare with the Earth's stratospheric polar vortices, it may also be useful to compare with the Earth's tropospheric polar vortex (upper tropospheric subtropical westerly jets) that forms at the poleward edge of the HC. As with Mars' vortices, there is a large increase in dθ/dp on the poleward side of Earth's subtropical jets, low PV equatorward of the jet (i.e., within the HC), and a large increase of PV poleward of the jet (Figure 14b). Despite these similarities, noticeable differences exist. Most obviously, Earth's subtropical jets and Mars' polar jet occur at different latitudes. Also, there is a monotonic increase of PV poleward of the Earth's subtropical jet and no off-pole local maximum, as both are found on Mars. The cause of this difference in PV between Mars and Earth is unknown and needs further investigation. One possibility is that it is related to differences in radiative processes (e.g., latent heating due to condensation of CO_2 within the Martian polar vortices, which has no equivalent on Earth).

7. Conclusions

Our analysis of version 1.0 of MACDA and a preliminary version of EMARS has shown that there is quantitative agreement between the reanalyses in the representation of the polar vortex in the lower atmosphere

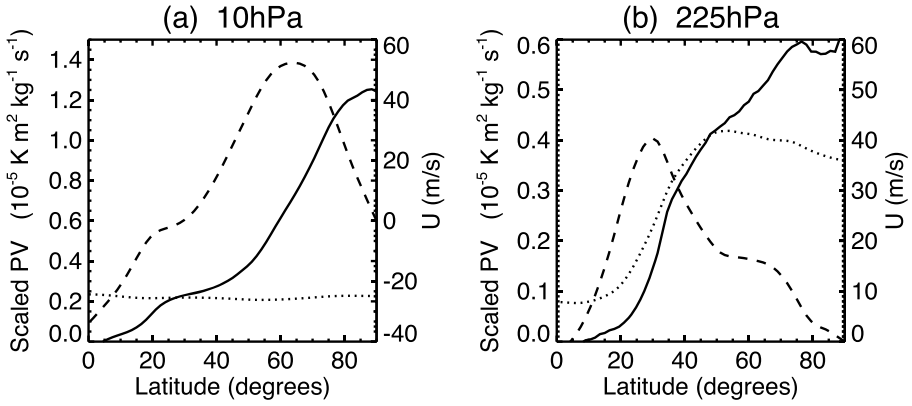

Figure 14. Monthly-mean zonal-mean scaled PV (solid curves), dθ/dp (dotted curves), and zonal winds (dashed curves) as a function of latitude on the (a) 10 hPa and (b) 225 hPa surfaces in Earth's atmosphere for January 2000 based on ERA-Interim reanalyses. dθ/dp is plotted on the PV scale and is multiplied by 0.01 first in Figure 14a.

(pressures greater than 0.1 hPa), where TES data are assimilated. This agreement occurs even though there are differences in the vortex structure in the free-running MGCMs used in each reanalysis. This shows the ability of the TES observations to constrain estimates of the circulation in the reanalyses and gives us confidence in the features in the lower atmosphere as represented in both of the reanalyses. There are, however, differences between the reanalyses at higher altitudes (where no data is assimilated), with these differences reflecting differences between the free-running MGCMs that are used in EMARS and MACDA. This indicates that differences between MGCMs drive the differences between the reanalyses at these altitudes and that caution is required when interpreting the upper atmosphere of the current versions of the reanalyses.

In both reanalyses there is a strong westerly jet in winter high latitudes that tilts toward the pole with height, with the NH winter jet stronger than that in the SH. They also show similar potential vorticity (PV) distributions, with low PV equatorward of the jet core, steepest meridional PV gradients poleward of the jet core, and latitude of maximum PV offset from the pole (in the lower atmosphere). The low values of PV in low and middle latitudes occur because there is approximately angular momentum conserving flow inside the near-global Hadley Cell, with the large increase in PV poleward of the jet due to a large increase in $d\theta/dp$ produced by the descending branch of the Hadley Cell. The occurrence of the steepest meridional PV gradients poleward of the jet core means that the size of the vortex is smaller if defined in terms of PV gradients rather than location of maximum zonal winds.

Maps of 30 sol mean PV show an elliptical annulus of high PV with the center near the pole and fairly constant area, shape, and orientation from fall to spring (as shown for MACDA by *Mitchell et al*. [2015]). However, on daily time scales the shape and orientation of the vortex is much more variable, and there is not a continuous annulus of PV but rather a series of smaller scale coherent regions of high PV. It is only when averaged over time (e.g., 30 sols) does the high PV appear as a near-continuous elliptical annulus.

The cause and stability of the PV annulus, and reality of small-scale PV features, are open questions and will be addressed in future studies using high-resolution simulations. Answering these will have implications for understanding the meridional transport of tracers, as more rapid horizontal mixing between middle latitudes, and the polar region may be expected if there is a ring of small-scale vortices rather than a continuous annulus.

The structure of potential vorticity in the Martian polar vortices described above is very different from that of Earth's stratospheric polar vortices. Much of this difference occurs because the Martian polar vortices are closely linked to Hadley Cell dynamics, whereas the Earth's stratospheric vortices are not directly linked to the Hadley Cell. We suggest that a more useful comparison may be between the Martian polar vortices and Earth's tropospheric polar vortices (middle latitude circumpolar westerlies). There are many similarities in the potential temperature and PV structure between these vortices, and more detailed comparisons may provide insight into the dynamics of both vortices.

Acknowledgments

We thank Dann Mitchell and Steven Thompson for helpful discussions and for sharing the code to calculate PV. The TES and MCS data are available in the Planetary Data System (PDS) http://pds-atmospheres.nmsu.edu/data_and_services/atmospheres_data/Mars/Mars.html. The MACDA v1,0 data set is available at 10.5285/78114093-E2BD-4601-8AE5-3551E62AEF2B, upon free registration to the Centre for Environmental Data Analysis (CEDA). All other data are available from the corresponding author upon direct request. This research was supported by NASA grants from the Mars Fundamental Research Program (NNX14AG53G) and Mars Data Analysis Program (NNX13AK02G). Development of EMARS was supported by NASA MDAP grants NNX11AL25G and NNX14AM13G.

References

Banfield, D., B. J. Conrath, M. D. Smith, P. R. Christensen, and R. J. Wilson (2003), Forced waves in the Martian atmosphere from MGS TES nadir data, *Icarus*, *161*, 319–345.

Banfield, D., B. J. Conrath, P. J. Gierasch, R. J. Wilson, and M. D. Smith (2004), Traveling waves in the Martian atmosphere from MGS TES nadir data, *Icarus*, *170*, 365–403.

Barnes, J. R., and R. M. Haberle (1996), The Martian zonal-mean circulation: Angular momentum and potential vorticity structure in GCM simulations, *J. Atmos. Sci.*, *53*, 3143–315.

Basu, S., R. J. Wilson, M. I. Richardson, and A. P. Ingersoll (2006), Simulation of spontaneous and variable global dust storms with the GFDL Mars GCM, *J. Geophys. Res.*, *111*, E09004, doi:10.1029/2005JE002660.

Clancy, R. T., and S. W. Lee (1991), A new look at dust and clouds in the Mars atmosphere: Analysis of emission-phase-function sequences from global Viking IRTM observations, *Icarus*, *93*, 135–158.

Clancy, R. T., M. J. Wolff, B. A. Whitney, B. A. Cantor, M. D. Smith, and T. H. McConnochie (2010), Extension of atmospheric dust loading to high altitudes during the 2001 Mars dust storm: MGS TES limb observations, *Icarus*, *207*, 98–109.

Clough, S. A., N. S. Grahame, and A. O'Neill (1985), Potential vorticity in the stratosphere derived using data from satellites, *Quart. J. Royal Meteorol. Soc.*, *111*, 335–358.

Dritschel, D. G., and L. M. Polvani (1992), The roll-up of vorticity strips on the surface of a sphere, *J. Fluid Mech.*, *234*, 47–69.

Forget, F., F. Hourdin, R. Fournier, C. Hourdin, O. Talagran, M. Collins, S. R. Lewis, P. L. Read, and J.-P. Huot (1999), Improved general circulation models of the Martian atmosphere from the surface to above 80 km, *J. Geophys. Res.*, *104*, 24,155–24,175, doi:10.1029/1999JE001025.

Greybush S. J., Wilson R. J., Hoffman R. N., Hoffman M. J., Miyoshi T., Ide K., McConnochie T., and Kalnay E. (2012), Ensemble Kalman filter data assimilation of Thermal Emission Spectrometer temperature retrievals into a Mars GCM, *J. Geophys. Res. 117*, E11008, doi:10.1029/2012JE004097.

Guzewich, S. D., E. R. Talaat, A. D. Toigo, D. W. Waugh, and T. H. McConnochie (2013), High-altitude dust layers on Mars: Observations with the Thermal Emission Spectrometer, *J. Geophys. Res. Planets*, *118*, 1177–1194, doi:10.1002/jgre.20076.
Guzewich, S. D., A. D. Toigo, and D. W. Waugh (2016), The effect of dust on the Mars polar vortices, *Icarus*, *278*, 100–118.
Hartmann, D. L. (1983), Barotropic instability of the polar night jet stream, *J. Atmos. Sci.*, *40*, 817–835.
Hoskins, B. J., McIntyre, M. E., and Robertson, A. W. (1985). On the use and significance of isentropic potential vorticity maps. *Quart. J. Royal Meteorol. Soc.*, *111*, 877–946.
Hunt, B. R., E. J. Kostelich, and I. Szunyogh (2007), Efficient data assimilation for spatiotemporal chaos: A local ensemble transform Kalman filter, *Physica D*, *230*, 112–126, doi:10.1016/j.physd.2006.11.008.
Held, I. M., and A. Y. Hou (1980), Nonlinear axially symmetric circulations in a nearly inviscid atmosphere, *J. Atmos. Sci.*, *37*, 515–533.
Ishioka, K., and S. Yoden (1994), Nonlinear evolution of a barotropically unstable circumpolar vortex, *J. Meteor. Soc. Jpn.*, *72*, 63–80.
Kleinböhl, A., et al. (2009), Mars Climate Sounder limb profile retrieval of atmospheric temperature, pressure, and dust and water ice opacity, *J. Geophys. Res.*, *114*, E10006, doi:10.1029/2009JE003358.
Lait, L. (1994), An alternative form for potential vorticity, *J. Atmos. Sci.*, *51*, 1754–1759.
Lorenc, A. C., R. S. Bell, and B. Macpherson (1991), The Meteorological Office analysis correction data assimilation scheme. *Quart. J. Royal Meteorol. Soc.*, *117*, 59–89.
Madeleine, J.-B., F. Forget, E. Millour, L. Montabone, and M. J. Wolff (2011), Revisiting the radiative impact of dust on Mars using the LMD Global Climate Model, *J. Geophys. Res.*, *116*, E11010, doi:10.1029/2011JE003855.
Madeleine, J.-B., F. Forget, E. Millour, T. Navarro, and A. Spiga (2012), The influence of radiatively active water ice clouds on the Martian climate, *Geophys. Res. Lett.*, *39*, L23202, doi:10.1092/2012GL053564.
McConnochie, T. H. (2011), Planetary wave breaking and the surf zone in the vicinity of the Martian Polar vortex, The Fourth International Workshop on the Mars Atmosphere: Modelling and observation, held 8-11 February, 2011, in Paris, France. [Available at http://www-mars.lmd.jussieu.fr/paris2011/program.html, pp. 136–138.]
McDunn, T., S. Bougher, J. Murphy, A. Kleinbohl, F. Forget, and M. Smith (2013), Characterization of middle-atmosphere polar warming at Mars, *J. Geophys. Res. Atmos.*, *118*, 161–178, doi:10.1002/jgre.20016.
Mitchell, D. M., L. Montabone, S. Thomson, and P. L. Read (2015), Polar vortices on Earth and Mars: A comparative study of the climatology and variability from reanalyses, *Q. J. R. Meteorol. Soc.*, doi:10.1002/qj.23.
Montabone, L., K. Marsh, S. R. Lewis, P. L. Read, M. D. Smith, J. Holmes, A. Spiga, D. Lowe, and A. Pamment (2014), The Mars Analysis Correction Data Assimilation (MACDA) Dataset V1.0, *Geosci. Data J.*, doi:10.1002/gdj3.13.
Montabone, L., F. Forget, E. Millour, R. J. Wilson, S. R. Lewis, D. Kass, A. Kleinböhl, M. T. Lemmon, M. D. Smith, and M. J. Wolff (2015), Eight-year climatology of dust optical depth on Mars, *Icarus*, doi:10.1016/j.icarus.2014.12.034.
Montmessin, F., F. Forget, P. Rannou, M. Cabane, and R. M. Haberle (2004), Origin and role of water ice clouds in the Martian water cycle as inferred from a general circulation model, *J. Geophys. Res.*, *109*, E10004, doi:10.1029/2004JE002284.
Richardson, M. I., and R. J. Wilson (2002), A topographically forced asymmetry in the Martian circulation and climate, *Nature*, *416*, 298–301.
Shirley, J. H., T. H. McConnochie, D. M. Kass, A. Kleinböhl, J. T. Schofield, N. G. Heavens, D. J. McCleese, J. Benson, D. P. Hinson, and J. L. Bandfield (2015), Temperatures and aerosol opacities of the Mars atmosphere at aphelion: Validation and inter-comparison of limb sounding profiles from MRO/MCS and MGS/TES, *Icarus*, *251*, 26–49, doi:10.1016/j.icarus.2014.05.011.
Smith, M. D. (2004), Interannual variability in TES atmospheric observations of Mars during 1999–2003, *Icarus*, *167*(1), 148–165, doi:10.1016/j.icarus.2003.09.010.
Smith, M. D. (2008), Spacecraft observations of the Martian atmosphere, *Ann. Rev. Earth Planetary Sci.*, *36*, 191–219.
Waugh, D. W., A. Sobel, and L. M. Polvani (2016), What is the polar vortex and how does it influence weather? *Bull. Am. Meteorol. Soc.*, doi:10.1175/BAMS-D-15-00212.1..
Wilson, R. J. (1997), A general circulation model simulation of the Martian polar warming, *Geophys. Res. Lett.*, *24*, 123–126, doi:10.1029/96GL03814.
Wilson, R. J. (2011), Dust cycle modeling with the GFDL Mars general circulation model, 4th International workshop on the Mars atmosphere: modeling and observations, Paris, February, 2011. [Available at http://www-mars.lmd.jussieu.fr/paris2011/abstracts/wilson_rj3_paris2011.pdf.]
Wilson, R. J., and K. Hamilton (1996), Comprehensive model simulation of thermal tides in the Martian atmosphere, *J. Atmos. Sci.*, *53*(9), 1290–1326.
Wilson, R. J., and S. D. Guzewich (2014), Influence of water ice clouds on nighttime tropical temperature structure as seen by the Mars Climate Sounder, *Geophys. Res. Lett.*, *41*, 3375–3381, doi:10.1002/2014GL060082.
Wilson, R. J., S. R. Lewis, L. Montabone, and M. D. Smith (2008), Influence of water ice clouds on Martian tropical atmospheric temperatures, *Geophys. Res. Lett.*, *35*, L07202, doi:10.1029/2007GL032405.
Zalucha, A. M., R. A. Plumb, and R. J. Wilson (2010), An analysis of the effect of topography on the Martian Hadley cells. *J. Atmos. Sci.*, *67*, 673–693.
Zhao, Y., S. J. Greybush, R. J. Wilson, R. N. Hoffman, and E. Kalnay (2015), Impact of assimilation window length on diurnal features in a Mars atmospheric analysis, *Tellus A*, *67*, 26,042, doi:10.3402/tellusa.v67.26042.